

This is a self-archived version of an original article. This version may differ from the original in pagination and typographic details.

Author(s): Bazhenov, Andrey; Honkala, Karoliina

Title: Globally Optimized Equilibrium Shapes of Zirconia-Supported Rh and Pt Nanoclusters : Insights into Site Assembly and Reactivity

Year: 2019

Version: Published version

Copyright: © 2019 American Chemical Society.

Rights: CC BY 4.0

Rights url: <https://creativecommons.org/licenses/by/4.0/>

Please cite the original version:

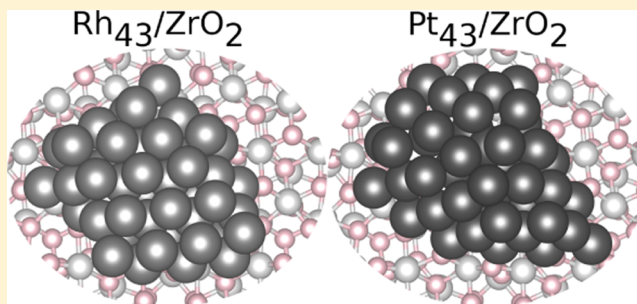
Bazhenov, A., & Honkala, K. (2019). Globally Optimized Equilibrium Shapes of Zirconia-Supported Rh and Pt Nanoclusters : Insights into Site Assembly and Reactivity. *Journal of Physical Chemistry C*, 123(12), 7209-7216. <https://doi.org/10.1021/acs.jpcc.9b00272>

Globally Optimized Equilibrium Shapes of Zirconia-Supported Rh and Pt Nanoclusters: Insights into Site Assembly and Reactivity

Andrey S. Bazhenov and Karoliina Honkala*

Department of Chemistry, Nanoscience Center, University of Jyväskylä, P.O. Box 35, FI-40014 Jyväskylä, Finland

ABSTRACT: Metal–support interfaces form an active site for many important catalytic reactions. The modeling of these interfacial sites calls for approximations to set up a structure model, which in turn may significantly have an impact on studied chemistry and obtained atomistic understanding. Herein, we have employed a density functional theory-based genetic approach to obtain globally optimized nanostructures for Rh and Pt clusters on a ZrO_2 support. The analysis of the obtained structures shows that Rh clusters take more compact shapes, whereas Pt prefers elongated and low-symmetry structures. We find that metal–oxide perimeter sites are structurally different, presenting varying Pt and Rh coordinations and CO adsorption energies. Our analysis shows that the presence of a support always destabilizes CO adsorption at the cluster edge, but the magnitude of destabilization varies substantially from site to site. The complexity of catalyst–support interactions demonstrates that even an inert support can intricately influence the reactivity of interfacial sites.



INTRODUCTION

Heterogeneous catalysts are indispensable for chemical industry in the production of fuels and commodity chemicals from a variety of feedstocks, and they typically comprise catalytically active metal nanoparticles dispersed on high surface area solid supports such as metal oxides. The activity and selectivity of a catalyst are intimately related to the size and shape of metal particles and the choice of support oxide, which can actively participate in chemical reactions or be an inert base.^{1–5} The support-induced changes in catalytic activity typically depends on the support material, and it is often attributed to perimeter sites at the metal–oxide interface,⁶ which can provide new binding geometries or favorable energetics for adsorbed species. The central role of the metal–oxide boundary has been recognized for many catalytic processes, especially for CO oxidation^{7–10} and water–gas-shift (WGS) reaction.^{11–14}

However, the structural characteristics of a metal–oxide interface and their influence on reaction rates at the atomic level remain typically elusive because of difficulties in experimental characterization. A frequently used approach to obtain an atomic-level description of a metal–oxide interface relies on density functional theory (DFT) calculations combined with a variety of different atomic structure models chosen to represent interfacial sites. Supported one-dimensional metal nanowires are popular particularly when chemical reactions are considered at the metal–oxide interfaces,^{7,14–19} while large, supported nanoparticle models are mainly employed to address catalyst–support interactions and charge transfer.²⁰ Recently, catalytic reaction studies^{12,21,22} have emerged on large nanoparticles, but they employ predefined particle morphologies.

Predefined interface structures are factitious, which in turn might influence their reactivity. Supported subnanometer clusters with varying shape, size, and chemical composition have been employed for a large number of supports and reactions.^{9,23–30} These cluster models traditionally build on manually generated structures emerging from chemical and physical intuition. While the number of choices for cluster morphology on a support is relatively small for few-atom clusters,³¹ the situation changes with an increasing number of atoms; therefore, the exploration of energetically low-lying atomic structures becomes a burdensome task and computationally impractical calling for automated methods. Advanced computational methods, such as basin hopping^{32,33} and evolutionary or genetic algorithms (GAs),^{34–36} have been recently developed and applied to search for globally optimized nanostructures in the gas phase^{37–41} and on support materials.^{42–45}

In the present work, we focus on the formation of the interfacial structures between monoclinic $\text{ZrO}_2(\bar{1}11)$ and Pt and Rh clusters. Both these metals demonstrate high activity in experiments, for example, for a WGS reaction,^{46–48} and $m\text{-ZrO}_2$ was chosen as it is a promising support material and known to have a bifunctional role in a WGS reaction.^{14,47–50}

We employ a first-principles-based GA approach to establish globally optimized nanostructures for Pt and Rh on $m\text{-ZrO}_2(\bar{1}11)$. GA was chosen as it provides an unbiased optimization scheme to determine a global minimum structure for oxide-supported metal clusters as shown, for example, for

Received: January 10, 2019

Revised: February 26, 2019

Published: February 26, 2019

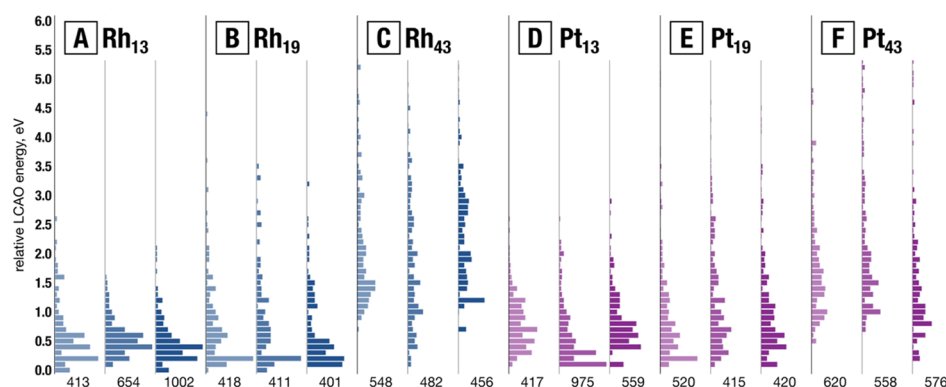


Figure 1. Number of screened structures for each GA run and cluster size for both metals together with the visualization of corresponding energy span. Relative LCAO energy is computed with respect to the most stable structure of each metal and size. A, B, and C stand for the Rh clusters of sizes 13, 19, and 43 atoms, whereas D, E, and F correspond to the Pt clusters of 13, 19, and 43 atoms, respectively.

Au clusters on $\text{TiO}_2(110)$ ⁴⁴ and $\text{MgO}(100)$.⁴³ Specifically, our aim is to determine the atomic structure of the metal–oxide interface and to explore how the interface structure depends on the chemical nature of metals and cluster sizes. Compared to $\text{TiO}_2(110)$ and $\text{MgO}(100)$ surfaces, the $\text{m-ZrO}_2(\bar{1}11)$ surface represents a lower symmetry structure with varying atom coordination numbers, which may affect the interface structure. Moreover, the size regime of metal clusters in the present work expands well beyond previously addressed 20-atom cluster sizes. Our results demonstrate that rhodium and platinum species have different affinity toward the oxide and, hence, exhibit different morphologies. With the largest, 43-atom cluster, we observe the emergence of a (111) facet at the boundary. The reactivity of perimeter sites at the formed metal–oxide interface is probed by evaluating the adsorption energy of carbon monoxide, a typical probe molecule used to explore reactivity in experiments.⁵¹ The analysis of coordination of interfacial sites highlights the uniqueness of these sites, which is also supported by the variation of CO binding energies.

COMPUTATIONAL DETAILS

Spin-paired calculations were carried out in the grid-based projector augmented wave (PAW) formalism of the DFT using the GPAW 1.1.0 code.^{52,53} The Perdew–Burke–Ernzerhof density functional was employed throughout the study.^{54,55} The core electrons of all atoms were represented with the PAW setups⁵⁶ in the frozen core approximation. The number of valence electrons for Rh and Pt was selected to be 9 and 10 electrons, respectively, to speed up the calculations. The impact of this choice is minor for obtained results, for example, CO adsorption energies on Pt(111) and Rh(111) surfaces are about the same as computed with 15 (Rh) and 16 (Pt) electron setups. In the structure search, the electron density was expanded in an atomic orbital basis set of double-zeta polarized quality.⁵⁷ At the refinement stage and for the adsorption studies, the electron density was represented on a real-space uniform grid [finite difference (FD)] with the maximum spacing of 200 mÅ to improve the accuracy. The reciprocal space was in all cases sampled by the Γ -point alone. All computational cells included at least 5 Å of vacuum below the slabs and at least 5 Å of vacuum above the slabs along the nonperiodic direction.

The structure search was performed using the GA implementation in the ASE package^{58,59} version (3.9.1). A (3

\times 3) $\text{m-ZrO}_2(\bar{1}11)$ slab of one stoichiometric layer thick was used as a template, with all atomic positions fixed. For each size and metal/oxide combination, three independent starting populations of 20 candidates were generated randomly. The offspring was created using cut-and-splice (70% probability) and mutation (30% probability) operators. Each candidate was relaxed with the threshold in the maximum residual force of 80 $\text{meV } \text{\AA}^{-1}$. A GA run was executed until its population stopped changing significantly and included ca. 400–800 structures.

The candidates in the three final populations were merged afterward and sorted by energy. The metal particles from 20 most stable structures were cut, placed onto the (3 \times 3) $\text{m-ZrO}_2(\bar{1}11)$ slabs of two stoichiometric layers thick (the atomic positions in the bottom layer fixed), and refined with the maximum residual force of 50 $\text{meV } \text{\AA}^{-1}$. Finally, the most stable structure among the refined was selected and used in further calculations and analyses.

Adhesion energy per atom in contact with the supports was computed as $\Delta E_{\text{adh}} = E_{\text{M/ZrO}_2(-111)} - E_{\text{M}} - E_{\text{ZrO}_2}$, where the subscript x refers to the number of atoms in a nanocluster. The first term is the energy of the globally optimized Rh or Pt cluster on the $\text{ZrO}_2(-111)$ surface, whereas the second term gives the energy of a gas-phase cluster obtained by removing a support and without optimizing the atomic structure. The third term stands for the energy of the support after removing a cluster and without optimizing the atomic structure. The adsorption of a CO molecule was only considered in the “on-top” position for perimeter sites along the metal–oxide interfaces (M/ZrO_2). The adsorption energy, ΔE_{ads} , was calculated using the energy of the gas-phase CO molecule, E_{CO} , as the reference ($12.8 \times 12.8 \times 12.8$ Å cell, 200 mÅ grid spacing, 50 $\text{meV } \text{\AA}^{-1}$ residual force threshold) as $\Delta E_{\text{ads}}^1 = E_{\Sigma} - (E_{\text{int}} + E_{\text{CO}})$, where E_{Σ} is the energy of a CO/M/ ZrO_2 system and E_{int} is the energy of a corresponding M/ ZrO_2 system. Adsorption energies for unsupported clusters were determined as follows: $\Delta E_{\text{ads}}^2 = E_{\text{CO/M}} - E_{\text{M}} - E_{\text{CO}}$, where $E_{\text{CO/M}}$ is the energy of the unsupported cluster obtained by removing ZrO_2 and fixing atoms into their optimized positions obtained in the presence of the support. E_{M} and E_{CO} are total energies of the bare cluster and gas-phase CO with all the atoms fixed to their optimized positions obtained in the presence of the support. $\Delta \Delta E_{\text{ads}} = \Delta E_{\text{ads}}^1 - \Delta E_{\text{ads}}^2$ describes the change in adsorption energy because of the support. The positive (negative) value of $\Delta \Delta E_{\text{ads}}$ corresponds to destabilization (stabilization) of CO binding because of ZrO_2 .

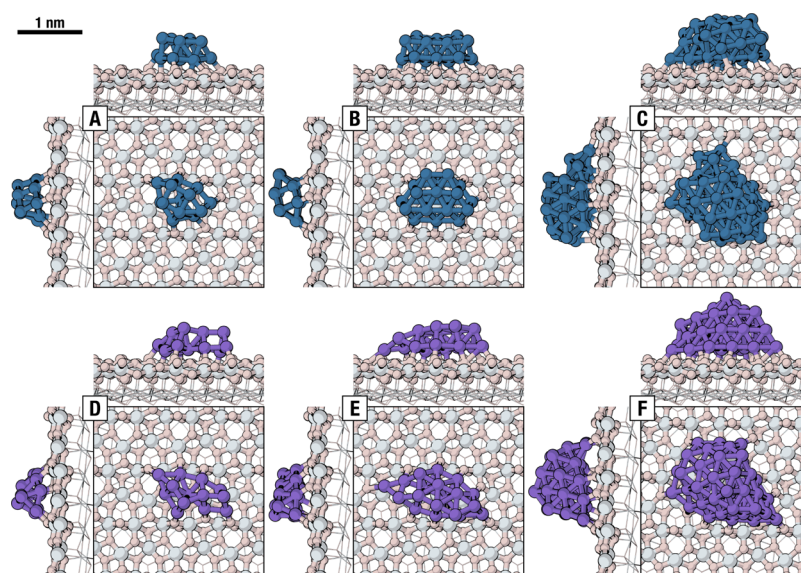


Figure 2. Globally optimized structures of (A) Rh₁₃, (B) Rh₁₉, (C) Rh₄₃, (D) Pt₁₃, (E) Pt₁₉, and (F) Pt₄₃ nanoclusters supported on the ZrO₂ surface slab. Each structure is shown in top, front, and side views. Color scheme: Rh in teal, Pt in purple, Zr in light gray, and O in pink. The fixed layers of the supporting oxide are shown in wireframe.

RESULTS AND DISCUSSION

In this study, we address three cluster sizes by considering M₁₃, M₁₉, and M₄₃ (M = Rh, Pt) metal clusters. The first two, M₁₃ and M₁₉, are, respectively, the smallest possible cuboctahedron and octahedron for the face-centered cubic metals. The last one, M₄₃, exhibits a distorted rhombicuboctahedral shape and may be constructed from the M₁₉ octahedrons by placing metal trimers onto each of the triangular facets.

Equilibrium shapes of M₁₃, M₁₉, and M₄₃ nanoclusters deposited onto the ZrO₂ support were obtained through global optimization employing the GA. For each M/ZrO₂ structure, we performed three optimization runs, each starting from a randomly generated population. The offspring was created using cut-and-splice crossover (70% probability) and rattle mutation (30% probability) operations. The supporting oxide was represented with a fixed two-dimensional slab of one stoichiometric layer thick to lower the computational burden. We used the globally optimized M₁₉/ZrO₂ structures as templates for M₄₃/ZrO₂ optimization, implying that only 24 of 43 metal atoms were involved in the crossover and mutation operations. We note that only the atoms in the supporting oxide were fixed in the corresponding DFT calculations.

Overall, we screened 9845 M/ZrO₂ structures, employing the linear combination of atomic orbitals (LCAO) DFT formalism (see [Computational Details](#) for more details). The resulting ranking of the screened structures is given in [Figure 1](#). The majority of the structures for M₁₃ and M₁₉ are found within 1.0 eV from the most stable structure (see [Figure 1A,B,D,E](#)). The distributions for M₄₃ nanoclusters, shown in [Figure 1C,F](#), tend to be wider compared to those for M₁₃ and M₁₉ nanoclusters, owing to the fact that they have M₁₉ “cores” excluded from the GA operations. For each M/ZrO₂ system, the results of the three individual GA runs were merged and 60 lowest energy structures were selected, which were then re-evaluated on a two-layer ZrO₂ slab using the FD DFT formalism (see [Computational Details](#) for more details). The best ranked structure of the 60 selected was considered globally optimized.

[Figure 2](#) shows the best globally optimized M₁₃/ZrO₂, M₁₉/ZrO₂, and M₄₃/ZrO₂ systems. It is clearly seen that the 13- and 19-atom Pt and Rh nanoclusters exhibit different morphologies on the ZrO₂ surface. Rhodium ([Figure 2A–C](#)) tends to form more compact structures, whereas platinum nanoclusters ([Figure 2D–F](#)) are more elongated and adjust to the surface structure of ZrO₂, suggesting that platinum wets ZrO₂ at a higher extent in the considered size regime. These differences are also supported by adhesion energies, which are more exothermic for Pt being -143 and -169 kJ/mol for 13- and 19-atom nanoclusters. The corresponding adhesion energies for Rh nanoclusters are -116 and -112 kJ/mol suggesting that the metal–support interaction is weaker for 13- and 19-atom Rh nanoclusters than for Pt. The difference between rhodium and platinum decreases for M₄₃ nanoclusters, as both Rh₄₃ and Pt₄₃ begin to form (111)-type facets, which are energetically the most stable facets for the face-centered cubic metals. The similarity between Rh and Pt morphology is also illustrated by similar adhesion energies which are -96 and -98 kJ/mol, respectively, and indicate comparable metal–support interaction. Interestingly, for all these structures, the number of metal atoms in contact with the zirconia support is larger for Pt than for Rh.

When a metal is deposited on an oxide, lattice parameter mismatch introduces strain, which can be made worse by the choice of a computational model, especially for periodic structures. Herein, the analysis of metal–metal distances shows that average Rh–Rh distances in Rh₁₃/ZrO₂, Rh₁₉/ZrO₂, and Rh₄₃/ZrO₂ are, respectively, 2.56 ± 0.12 , 2.62 ± 0.11 , and 2.67 ± 0.11 Å being ca. 2–6% shorter compared to the Rh–Rh distance in the Rh bulk (2.73 Å). Similarly, for Pt₁₃/ZrO₂, Pt₁₉/ZrO₂, and Pt₄₃/ZrO₂, the average Pt–Pt distances are correspondingly 2.64 ± 0.09 , 2.685 ± 0.11 , and 2.70 ± 0.10 Å, respectively, which are ca. 4–6% shorter compared to the Pt–Pt distance in the Pt bulk (2.82 Å). The observed decrease in Pt–Pt and Rh–Rh distances results likely from clusters adjusting their structures to the surface structure of the oxide, and similar contraction with respect to bulk has been

seen computationally for, for example, Pt₁₃ on Al₂O₃²⁵ and experimentally for γ -alumina-supported Pt.⁶⁰

The metal nanoclusters are coordinated with the support by making M–Zr and M–O bonds, which is reflected in density of states plots (figure not provided), where the states of the nanocluster are partly placed into the gap of ZrO₂ and partly hybridized with the valence states of Zr and O atoms. According to the Bader charge analysis,⁶¹ the M/ZrO₂ systems exhibit mild charge transfer, the total magnitude of which is <0.5 electrons regardless of the size of the metal nanocluster and indicates that clusters remain metallic on ZrO₂. The difference between rhodium and platinum is found in the direction of charge transfer: rhodium acts as a weak electron donor with respect to the ZrO₂ support, whereas platinum is a weak electron acceptor. It is interesting to note that the Bader analysis shows that on TiO₂(110) Pt clusters are electron donors.⁶²

Upon cluster interaction with the support, a metal–oxide interface emerges, presenting perimeter sites. We define a perimeter site as a metal atom in a nanocluster, which is chemically bound to the supporting oxide and is accessible to adsorbates. Different morphologies exhibited by different nanoclusters suggest that the perimeter sites should also be different. We performed a comparative analysis of the first coordination spheres of the perimeter sites. As seen from Table 1, the perimeter sites in the studied systems have different

Table 1. First Coordination Spheres of the Perimeter Sites (Atoms) in M/ZrO₂ Systems^a

coordination	c.n.	Rh ₁₃	Rh ₁₉	Rh ₄₃	Pt ₁₃	Pt ₁₉	Pt ₄₃
M3 Zr1 O1	5				1	1	1
M3 Zr2 O0	5					1	
M3 Zr2 O1	6	1		1	1		1
M3 Zr3 O1	7				1		1
M4 Zr1 O1	6	1				2	
M4 Zr2 O1	7		1		1	1	
M4 Zr3 O1	8	1	1	2	1		2
M5 Zr1 O1	7	1	1			1	
M5 Zr2 O1	8	1	3	4			2
M5 Zr3 O1	9	1			3		1
M6 Zr1 O0	7			1			
M6 Zr2 O1	9						4
M6 Zr3 O1	10	1	1				
M7 Zr2 O1	10					1	
\sum_{sites}		7	7	8	8	7	8

^aThe number after M (Rh or Pt), Zr, and O refers to the coordination of that particular element.

coordinations, making them unique. If only the coordination to Pt or Rh atoms in perimeter sites is considered, Pt nanoclusters have more three-coordinated Pt atoms, whereas Rh nanoclusters present more five-coordinated metal atoms.

Having determined the GA structures for ZrO₂-supported Pt and Rh clusters with different sizes, we now focus on the systematic examination of CO adsorption characteristics. CO was chosen as a probe molecule because interfacial atoms have been identified as active sites, for example, for water–gas-shift reaction.^{12,14,16,63–66}

Figure 3 shows the adsorption energies of a CO molecule in the “on-top” geometry for all perimeter sites in each studied system. Overall, the CO binding is moderately exothermic, but adsorption strength varies from site to site, further supporting

the uniqueness of the perimeter sites in the considered clusters. On average, we find the calculated adsorption energies to be $-(147 \pm 16)$, $-(164 \pm 17)$, and $-(176 \pm 19)$ kJ mol^{−1} for Rh₁₃/ZrO₂, Rh₁₉/ZrO₂, and Rh₄₃/ZrO₂, respectively. In the case of Pt-based systems, the variation of the energy values is larger being $-(152 \pm 33)$, $-(171 \pm 31)$, and $-(138 \pm 31)$ kJ mol^{−1} for Pt₁₃/ZrO₂, Pt₁₉/ZrO₂, and Pt₄₃/ZrO₂, respectively. The more pronounced variation of adsorption energy on Pt clusters could be in part due to their lower symmetry and a larger number of low Pt-coordinated perimeter sites. Interestingly, similar large variation in CO adsorption energies has been reported on the perimeter sites of a MgO-supported elongated Pt₁₃ cluster, whereas on the interfacial sites of a spherical Pt₁₃ cluster adsorption energies are more identical.⁶⁷

The strongest binding modes of a CO molecule for each system are given in Figure 4, which shows that the variation in most exothermic adsorption energies is negligible for different Pt cluster sizes despite different coordinations of a metal atom bound to CO, while slightly larger variation is seen for Rh. The bond lengths of adsorbed CO are independent of the cluster size being on average 1.164 and 1.157 Å for Rh and Pt perimeter sites, respectively. The differences to the bond lengths of atop-bound CO on the Rh(111) and Pt(111) surfaces are minor. Overall, the most exothermic CO adsorption energies on a top geometry of supported metal clusters are close to the values computed on Rh(111) and Pt(111) surfaces, where adsorption energies are -185 and -174 kJ/mol, respectively, at the 2×2 surface cell. In addition, CO adsorption energy on Pt₄₃/ZrO₂ differs only by 2 kJ/mol from the value reported for an ideal gas-phase cuboctahedron Pt₃₈ nanocluster.⁶⁸

To further explore the origin of the variation in CO adsorption energies, we analyzed the role of the support in more detail. In the present case, the oxide surface is inhomogeneous in a sense that the cations and anions do not form a highly symmetrical lattice and their coordination numbers vary. Therefore, the influence of the support might differ from one perimeter site to the other. The CO adsorption geometry and cluster geometry have been optimized in the presence of the support, whereas the unsupported structures have been obtained by removing the support and keeping the metal atoms and CO fixed. This approach excludes the influence of quite substantial gas-phase cluster deformation on studied energies. $\Delta\Delta E_{\text{ads}}$ measures explicit support influence on CO binding and is plotted in Figure 5a. Only positive $\Delta\Delta E_{\text{ads}}$ values have been obtained, which means that the support destabilizes CO adsorption in all studied systems. However, the magnitude of destabilization ranges from 5 to 86 kJ/mol and varies from site to site, further highlighting the uniqueness of the interfacial sites. On average, the magnitudes of destabilization are 65, 43, 39, and 37 kJ/mol/site for Pt₁₃, Pt₁₉, Rh₁₃, and Rh₁₉ clusters, respectively. As an example, we explicitly compare CO binding energies between Pt₁₉ and Rh₁₉ clusters with and without the support in Figure 5b. The plot highlights larger variation for CO binding on unsupported Pt₁₉ than for Rh₁₉ and suggests that for given cluster sizes and shapes the finite size effects are more pronounced for Pt than for Rh. We associate this to a lower symmetry of Pt compared to Rh, rather than the chemical nature of the metal. Furthermore, the variation in CO adsorption energy on ZrO₂-supported Rh₁₉ is mainly due to the support. For example, sites 2, 3, and 4 have nearly equal binding strengths on unsupported Rh₁₉, but in the presence of the support site 3

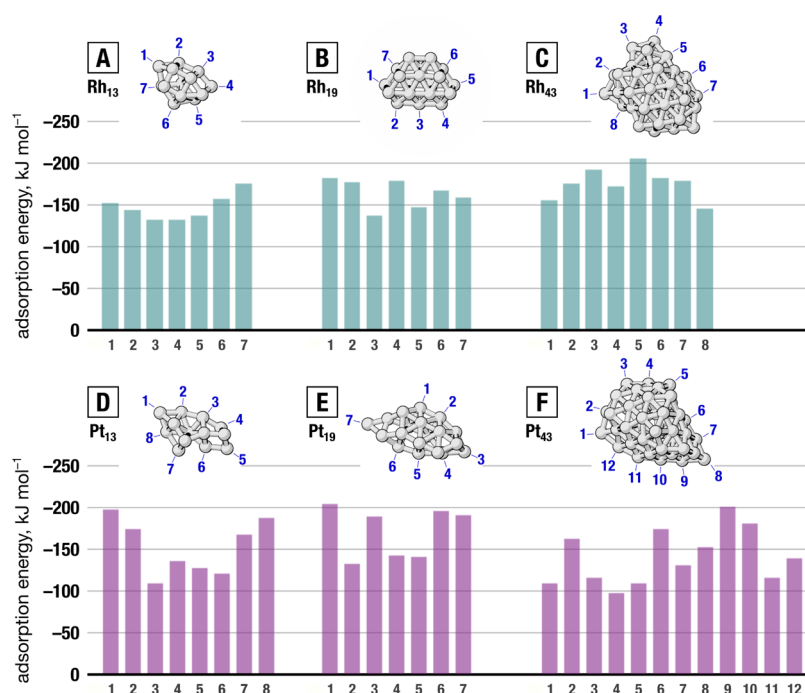


Figure 3. Considered CO adsorption sites numbered at the M-oxide boundary (support not shown) and CO adsorption energies plotted for each site, on Rh₁₃ (A), Rh₁₉ (B), Rh₄₃ (C), Pt₁₃ (A), Pt₁₉ (E), Pt₄₃ (F) clusters.

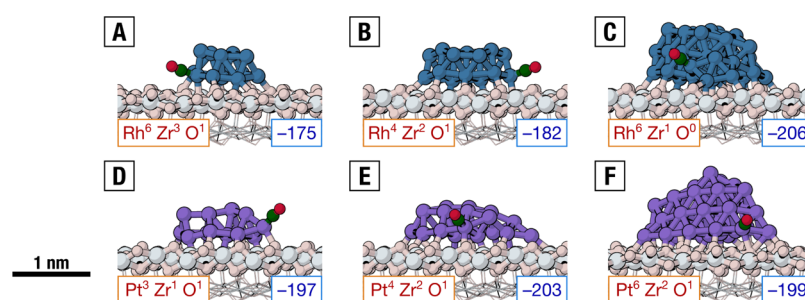


Figure 4. Most favorable adsorption of a CO molecule onto the perimeter sites of (A) Rh₁₃/ZrO₂, (B) Rh₁₉/ZrO₂, (C) Rh₄₃/ZrO₂, (D) Pt₁₃/ZrO₂, (E) Pt₁₉/ZrO₂, and (F) Pt₄₃/ZrO₂. The corresponding adsorption energies (in kJ mol^{-1}) are given in the bottom right corners of the panels. The coordination of the corresponding perimeter sites in the absence of CO is given in the bottom left corner of the panels. Color scheme: Rh in teal, Pt in purple, Zr in light gray, oxide O in pink, and CO in green and red. The fixed layers of the supporting oxide are shown in wireframe.

binds CO considerably weaker than the other two sites. In the case of Pt₁₉/ZrO₂, the variation in CO adsorption energy is partly due to the fluctuation in support influence and also due to the changes in CO binding energies on an unsupported cluster. For example, site 4 which initially binds CO strongly experiences large steric repulsion from the support, whereas site 5 binds CO weakly but has only small destabilization because of the support and thus in the presence of the support these two sites have nearly equal CO binding energies. Altogether, our results show that the reactivity of interfacial sites toward CO adsorption depends sensitively not only on the local geometry of the zirconia support below but also on the shape of the cluster.

CONCLUSIONS

In summary, the ability to computationally determine global minimal structures for supported metal clusters is important to determine metal–support interfacial sites whose structural and electronic characteristics determine their catalytic properties. Herein, we obtained the GA structures for 13-, 19-, and 43-

atom Pt and Rh clusters on m-ZrO₂(−111). Our results highlight that Rh and Pt exhibit different shapes on the studied oxide surface: Rh clusters are more rounded, and Pt clusters present more elongated shapes. With the M₄₃ cluster, we see the emergence of the (111)-type facets for both metals and demonstrate that (111)/oxide models typically used in DFT calculations are structurally correct, but periodic boundary conditions may introduce artificial strain effects. The analysis of coordination of perimeter sites shows that they are structurewise unique for both metals and studied sizes; this is reflected through the variation of CO adsorption energies for different boundary sites. However, for the best Pt interfacial site at each cluster size, CO adsorption energy is nearly constant, whereas slightly larger changes are seen for Rh clusters. Our analysis highlights that the variation in CO adsorption energy in the studied size regime results from site-dependent catalyst–support interactions combined with the finite size effects. Overall, the first-principles GA approach is a valuable methodology to obtain globally minimal structures for small clusters supported, but high computational burden for larger nanostructures such as M₄₃ calls for further methodology

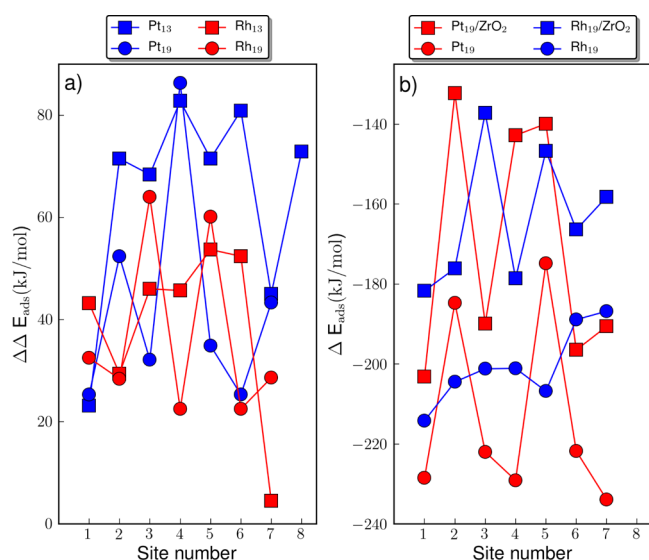


Figure 5. Comparison of (a) $\Delta\Delta E_{\text{ads}}$ for 13- and 19-atom Rh and Pt clusters and (b) adsorption energies for supported and unsupported Pt₁₉ and Rh₁₉ clusters. Site numbers are taken from Figure 3.

development employing, for example, neural networks to reach the experimentally important size regime in the future.

AUTHOR INFORMATION

Corresponding Author

*E-mail: karoliina.honkala@jyu.fi

ORCID

Karoliina Honkala: 0000-0002-3166-1077

Notes

The authors declare no competing financial interest.

ACKNOWLEDGMENTS

This work is funded by the Academy of Finland (<https://www.aka.fi/en/>, grant 277222). The electronic structure calculations were made possible by the computational Grand Challenge project provided by the CSC—IT Center for Science, Espoo, Finland (<https://www.csc.fi/en/>). Both A.S.B. and K.H. thank Prof. B. Hammer for fruitful discussions, and A.S.B. is also grateful for the hospitality during his visit in Aarhus.

REFERENCES

- Schauermann, S.; Nilius, N.; Shaikhutdinov, S.; Freund, H.-J. Nanoparticles for Heterogeneous Catalysis: New Mechanistic Insights. *Acc. Chem. Res.* **2013**, *46*, 1673–1681.
- Cuenya, B. R.; Beharfarid, F. Nanocatalysis: Size- and Shape-Dependent Chemisorption and Catalytic Reactivity. *Surf. Sci. Rep.* **2015**, *70*, 135–187.
- Liu, L.; Corma, A. Metal Catalysts for Heterogeneous Catalysis: From Single Atoms to Nanoclusters and Nanoparticles. *Chem. Rev.* **2018**, *118*, 4981–5079.
- Ro, I.; Resasco, J.; Christopher, P. Approaches for Understanding and Controlling Interfacial Effects in Oxide-Supported Metal Catalysts. *ACS Catal.* **2018**, *8*, 7368–7387.
- Stoyanovskii, V. O.; Vedyagin, A. A.; Aleshina, G. I.; Volodin, A. M.; Noskov, A. S. Characterization of Rh/Al₂O₃ Catalysts After Calcination at High Temperatures under Oxidizing Conditions by Luminescence Spectroscopy and Catalytic Hydrogenolysis. *Appl. Catal., B* **2009**, *90*, 141–146.
- Hayek, K.; Kramer, R.; Pál, Z. Metal-Support Boundary Sites in Catalysis. *Appl. Catal., A* **1997**, *162*, 1–15.

- Green, I. X.; Tang, W.; Neurock, M.; Yates, J. T. Low-Temperature Catalytic H₂ Oxidation over Au Nanoparticle/TiO₂ Dual Perimeter Sites. *Angew. Chem., Int. Ed.* **2011**, *50*, 10186–10189.
- Cargnello, M.; Doan-Nguyen, V. V. T.; Gordon, T. R.; Diaz, R. E.; Stach, E. A.; Gorte, R. J.; Fornasiero, P.; Murray, C. B. Control of Metal Nanocrystal Size Reveals Metal-Support Interface Role for Ceria Catalysts. *Science* **2013**, *341*, 771–773.
- Saavedra, J.; Doan, H. A.; Pursell, C. J.; Grabow, L. C.; Chandler, B. D. The Critical Role of Water at the Gold-Titania Interface in Catalytic CO Oxidation. *Science* **2014**, *345*, 1599–1602.
- Vedyagin, A. A.; Volodin, A. M.; Kenzhin, R. M.; Stoyanovskii, V. O.; Shubin, Y. V.; Plyusnin, P. E.; Mishakov, I. V. Effect of Metal-Metal and Metal-Support Interaction on Activity and Stability of Pd-Rh/alumina in CO Oxidation. *Catal. Today* **2017**, *293–294*, 73–81.
- Park, J. B.; Graciani, J.; Evans, J.; Stacchiola, D.; Senanayake, S. D.; Barrio, L.; Liu, P.; Sanz, J. F.; Hrbek, J.; Rodriguez, J. A. Gold, Copper, and Platinum Nanoparticles Dispersed on CeOx/TiO₂(110) Surfaces: High Water-Gas Shift Activity and the Nature of the Mixed-Metal Oxide at the Nanometer Level. *J. Am. Chem. Soc.* **2010**, *132*, 356–363.
- Foppa, L.; Margossian, T.; Kim, S. M.; Müller, C.; Copéret, C.; Larmier, K.; Comas-Vives, A. Contrasting the Role of Ni/Al₂O₃ Interfaces in Water-Gas Shift and Dry Reforming of Methane. *J. Am. Chem. Soc.* **2017**, *139*, 17128–17139.
- Shekhar, M.; Wang, J.; Lee, W.-S.; Williams, W. D.; Kim, S. M.; Stach, E. A.; Miller, J. T.; Delgass, W. N.; Ribeiro, F. H. Size and Support Effects for the Water-Gas Shift Catalysis over Gold Nanoparticles Supported on Model Al₂O₃ and TiO₂. *J. Am. Chem. Soc.* **2012**, *134*, 4700–4708.
- Kauppinen, M. M.; Melander, M. M.; Bazhenov, A. S.; Honkala, K. Unraveling the Role of the Rh/ZrO₂ Interface in the Water-Gas Shift Reaction via a First Principles microkinetic study. *ACS Catal.* **2018**, *8*, 11633–11647.
- Sun, K.; Kohyama, M.; Tanaka, S.; Takeda, S. Reaction Mechanism of the Low-Temperature Water–Gas Shift Reaction on Au/TiO₂ Catalysts. *J. Phys. Chem. C* **2017**, *121*, 12178–12187.
- Zhao, Z.-J.; Li, Z.; Cui, Y.; Zhu, H.; Schneider, W. F.; Delgass, W. N.; Ribeiro, F.; Greeley, J. Importance of Metal-Oxide Interfaces in Heterogeneous Catalysis: A Combined DFT, Microkinetic, and Experimental Study of Water-Gas Shift on Au/MgO. *J. Catal.* **2017**, *345*, 157–169.
- Tang, Q.-L.; Liu, Z.-P. Identification of the Active Cu Phase in the Water-Gas Shift Reaction over Cu/ZrO₂ from First Principles. *J. Phys. Chem. C* **2010**, *114*, 8423–8430.
- Mehta, P.; Greeley, J.; Delgass, W. N.; Schneider, W. F. Adsorption Energy Correlations at the Metal–Support Boundary. *ACS Catal.* **2017**, *7*, 4707–4715.
- Duan, Z.; Henkelman, G. Calculations of CO Oxidation over a Au/TiO₂ Catalyst: A Study of Active Sites, Catalyst Deactivation, and Moisture Effects. *ACS Catal.* **2018**, *8*, 1376–1383.
- Kozlov, S. M.; Neyman, K. M. Effects of Electron Transfer in Model Catalysts Composed of Pt Nanoparticles on CeO₂(111) Surface. *J. Catal.* **2016**, *344*, 507–514.
- Molina, L. M.; Hammer, B. Theoretical Study of CO Oxidation on Au Nanoparticles Supported by MgO(100). *Phys. Rev. B: Condens. Matter Mater. Phys.* **2004**, *69*, 155424.
- Silaghi, M.-C.; Comas-Vives, A.; Copéret, C. CO₂ Activation on Ni/γ-Al₂O₃ Catalysts by First-Principles Calculations: From Ideal Surfaces to Supported Nanoparticles. *ACS Catal.* **2016**, *6*, 4501–4505.
- Vajda, S.; Pellin, M. J.; Greeley, J. P.; Marshall, C. L.; Curtiss, L. A.; Ballentine, G. A.; Elam, J. W.; Catillon-Mucherie, S.; Redfern, P. C.; Mehmood, F.; et al. Subnanometre Platinum Clusters as Highly Active and Selective Catalysts for the Oxidative Dehydrogenation of Propane. *Nat. Mater.* **2009**, *8*, 213–216.
- Aranifard, S.; Ammal, S. C.; Heyden, A. On the Importance of Metal–Oxide Interface Sites for the Water-Gas Shift Reaction over Pt/CeO₂ Catalysts. *J. Catal.* **2014**, *309*, 314–324.

- (25) Hu, C. H.; Chizallet, C.; Mager-Maury, C.; Corral-Valero, M.; Sautet, P.; Toulhoat, H.; Raybaud, P. Modulation of Catalyst Particle Structure upon Support Hydroxylation: Ab initio Insights into Pd_{13} and $\text{Pt}_{13}/\gamma\text{-Al}_2\text{O}_3$. *J. Catal.* **2010**, *274*, 99–110.
- (26) Frondelius, P.; Häkkinen, H.; Honkala, K. Formation of Gold(I) Edge Oxide at Flat Gold Nanoclusters on an Ultrathin MgO Film under Ambient Conditions. *Angew. Chem., Int. Ed.* **2010**, *49*, 7913–7916.
- (27) Honkala, K. Tailoring Oxide Properties: an Impact on Adsorption Characteristics of Molecules and Metals. *Surf. Sci. Rep.* **2014**, *69*, 366–388.
- (28) Baxter, E. T.; Ha, M.-A.; Cass, A. C.; Alexandrova, A. N.; Anderson, S. L. Ethylene Dehydrogenation on Pt_{478} Clusters on $\gamma\text{-Al}_2\text{O}_3$ Strong Cluster Size Dependence Linked to Preferred Catalyst Morphologies. *ACS Catal.* **2017**, *7*, 3322–3335.
- (29) Larmier, K.; Liao, W.-C.; Tada, S.; Lam, E.; Verel, R.; Bansode, A.; Urakawa, A.; Comas-Vives, A.; Copéret, C. CO_2 -to-Methanol Hydrogenation on Zirconia-Supported Copper Nanoparticles: Reaction Intermediates and the Role of the Metal–Support Interface. *Angew. Chem., Int. Ed.* **2017**, *56*, 2318–2323.
- (30) Suchorski, Y.; Kozlov, S. M.; Bespalov, I.; Datler, M.; Vogel, D.; Budinska, Z.; Neyman, K. M.; Rupprechter, G. The Role of Metal/Oxide Interfaces for Long-Range Metal Particle Activation During CO Oxidation. *Nat. Mater.* **2018**, *17*, 519–522.
- (31) Frondelius, P.; Häkkinen, H.; Honkala, K. Adsorption of Gold Clusters on Metal-Supported MgO: Correlation to Electron Affinity of Gold. *Phys. Rev. B: Condens. Matter Mater. Phys.* **2007**, *76*, 073406.
- (32) Wales, D. J.; Doye, J. P. K. Global Optimization by Basin-Hopping and the Lowest Energy Structures of Lennard-Jones Clusters Containing up to 110 Atoms. *J. Phys. Chem. A* **1997**, *101*, 5111.
- (33) Wales, D. J.; Scheraga, H. A. Global Optimization of Clusters, Crystals, and Biomolecules. *Science* **1999**, *285*, 1368.
- (34) Oganov, A. R.; Glass, C. W. Crystal Structure Prediction Using Ab Initio Evolutionary Techniques: Principles and Applications. *J. Chem. Phys.* **2006**, *124*, 244704.
- (35) Vilhelmsen, L. B.; Hammer, B. A Genetic Algorithm for First Principles Global Structure Optimization of Supported Nano Structures. *J. Chem. Phys.* **2014**, *141*, 044711.
- (36) Le, T. C.; Winkler, D. A. Discovery and Optimization of Materials Using Evolutionary Approaches. *Chem. Rev.* **2016**, *116*, 6107–6132.
- (37) Alexandrova, A. N.; Boldyrev, A. I.; Fu, Y.-J.; Yang, X.; Wang, X.-B.; Wang, L.-S. Structure of the $\text{Na}_x\text{Cl}_{x+1}-1$ ($x = 1-4$) Clusters via Ab Initio Genetic Algorithm and Photoelectron Spectroscopy. *J. Chem. Phys.* **2004**, *121*, 5709–5719.
- (38) Logsdail, A. J.; Li, Z. Y.; Johnston, R. L. Development and Optimization of a Novel Genetic Algorithm for Identifying Nano-clusters from Scanning Transmission Electron Microscopy Images. *J. Comput. Chem.* **2012**, *33*, 391–400.
- (39) Lysgaard, S.; Mýrdal, J. S. G.; Hansen, H. A.; Vegge, T. A DFT-Based Genetic Algorithm Search for AuCu Nanoalloy Electrocatalysts for CO_2 Reduction. *Phys. Chem. Chem. Phys.* **2015**, *17*, 28270–28276.
- (40) Shayeghi, A.; Götz, D.; Davis, J. B. A.; Schäfer, R.; Johnston, R. L. Pool-BCGA: a Parallelised Generation-Free Genetic Algorithm for the Ab Initio Global Optimisation of Nanoalloy Clusters. *Phys. Chem. Chem. Phys.* **2015**, *17*, 2104–2112.
- (41) Jäger, M.; Schäfer, R.; Johnston, R. L. First Principles Global Optimization of Metal Clusters and Nanoalloys. *Adv. Phys.: X* **2018**, *3*, S100009.
- (42) Panosetti, C.; Krautgasser, K.; Palagin, D.; Reuter, K.; Maurer, R. J. Global Materials Structure Search with Chemically Motivated Coordinates. *Nano Lett.* **2015**, *15*, 8044–8048.
- (43) Vilhelmsen, L. B.; Hammer, B. Systematic Study of Au_6 and Au_{12} Gold Clusters on $\text{MgO}(100)\text{F}$ Centers Using Density-Functional Theory. *Phys. Rev. Lett.* **2012**, *108*, 126101.
- (44) Vilhelmsen, L. B.; Hammer, B. Identification of the Catalytic Site at the Interface Perimeter of Au Clusters on TiO_2 . *ACS Catal.* **2014**, *4*, 1626–1631.
- (45) Paz-Borbón, L. O.; López-Martínez, A.; Garzón, I. L.; Posada-Amarillas, A.; Grönbeck, H. 2D–3D Structural Transition in Sub-Nanometer Pt_N Clusters Supported on $\text{CeO}_2(111)$. *Phys. Chem. Chem. Phys.* **2017**, *19*, 17845–17855.
- (46) Thion, O.; Diehl, F.; Avenier, P.; Schuurman, Y. Screening of Bifunctional Water-Gas Shift Catalysts. *Catal. Today* **2008**, *137*, 29–35.
- (47) Graf, P. O.; de Vlieger, D. J. M.; Mojet, B. L.; Lefferts, L. New Insight in Reactivity of Hydroxyl Groups in Water Gas Shift Reaction on Pt/ZrO_2 . *J. Catal.* **2009**, *262*, 181–187.
- (48) Tibiletti, D.; Meunier, F.; Goguet, A.; Reid, D.; Burch, R.; Boaro, M.; Vicario, M.; Trovarelli, A. An Investigation of Possible Mechanisms for the Water–Gas Shift Reaction over a ZrO_2 -Supported Pt Catalyst. *J. Catal.* **2006**, *244*, 183–191.
- (49) Azzam, K.; Babich, I.; Seshan, K.; Lefferts, L. Bifunctional Catalysts for Single-Stage Water–Gas Shift Reaction in Fuel Cell Applications. Part 1. Effect of the Support on the Reaction Sequence. *J. Catal.* **2007**, *251*, 153–162.
- (50) Hakeem, A. A.; Vásquez, R. S.; Rajendran, J.; Li, M.; Berger, R. J.; Delgado, J. J.; Kapteijn, F.; Makkee, M. The Role of Rhodium in the Mechanism of the Water-Gas Shift over Zirconia Supported Iron Oxide. *J. Catal.* **2014**, *313*, 34–45.
- (51) Lamberti, C.; Zecchina, A.; Groppo, E.; Bordiga, S. Probing the Surfaces of Heterogeneous Catalysts by in situ IR Spectroscopy. *Chem. Soc. Rev.* **2010**, *39*, 4951–5001.
- (52) Mortensen, J. J.; Hansen, L. B.; Jacobsen, K. W. Real-Space Grid Implementation of Projector Augmented Wave Method. *Phys. Rev. B: Condens. Matter Mater. Phys.* **2005**, *71*, 035109.
- (53) Enkovaara, J.; Rostgaard, C.; Mortensen, J. J.; Chen, J.; Dulak, M.; Ferrighi, L.; Gavnholt, J.; Glinsvad, C.; Haikola, V.; Hansen, H. A.; et al. Electronic Structure Calculations with GPAW: a Real-Space Implementation of the Projector Augmented-Wave Method". *J. Phys.: Condens. Matter* **2010**, *22*, 253202.
- (54) Perdew, J. P.; Burke, K.; Ernzerhof, M. Generalized Gradient Approximation Made Simple. *Phys. Rev. Lett.* **1996**, *77*, 3865–3868.
- (55) Perdew, J. P.; Burke, K.; Ernzerhof, M. Generalized Gradient Approximation Made Simple [Phys. Rev. Lett. 77, 3865 (1996)]. *Phys. Rev. Lett.* **1997**, *78*, 1396.
- (56) Blöchl, P. E. Projector Augmented Wave Method. *Phys. Rev. B: Condens. Matter Mater. Phys.* **1994**, *50*, 17953–17979.
- (57) Larsen, A. H.; Vanin, M.; Mortensen, J. J.; Thygesen, K. S.; Jacobsen, K. W. Localized Atomic Basis Set in the Projector Augmented Wave Method. *Phys. Rev. B: Condens. Matter Mater. Phys.* **2009**, *80*, 195112.
- (58) Bahn, S. R.; Jacobsen, K. W. An Object-Oriented Scripting Interface to a Legacy Electronic Structure Code. *Comput. Sci. Eng.* **2002**, *4*, 56–66.
- (59) Larsen, A. H.; Mortensen, J. J.; Blomqvist, J.; Castelli, I. E.; Christensen, R.; Dulak, M.; Friis, J.; Groves, M. N.; Hammer, B.; Hargus, C.; et al. The Atomic Simulation Environment—a Python Library for Working with Atoms. *J. Phys.: Condens. Matter* **2017**, *29*, 273002.
- (60) Pingel, T. N.; Jørgensen, M.; Yankovich, A. B.; Grönbeck, H.; Olsson, E. Influence of Atomic Site-Specific Strain on Catalytic Activity of Supported Nanoparticles. *Nat. Commun.* **2018**, *9*, 2722.
- (61) Henkelman, G.; Arnaldsson, A.; Jónsson, H. Bader A fast and robust algorithm for Bader decomposition of charge density. *Comput. Mater. Sci.* **2006**, *36*, 354.
- (62) Ammal, S. C.; Heyden, A. Nature of Pt_n/TiO_2 Interface Under Water-Gas shift Reaction Conditions: A Constrained Ab Initio Thermodynamics Study. *J. Phys. Chem. C* **2011**, *115*, 19246–19259.
- (63) Grenoble, D.; Estadt, M.; Ollis, D. The Chemistry and Catalysis of the Water Gas Shift Reaction: 1. The Kinetics Over Supported Metal Catalysts. *J. Catal.* **1981**, *67*, 90–102.
- (64) Panagiotopoulou, P.; Kondarides, D. I. Effect of the Nature of the Support on the Catalytic Performance of Noble Metal Catalysts for the Water–Gas Shift Reaction. *Catal. Today* **2006**, *112*, 49–52.
- (65) Thion, O.; Diehl, F.; Avenier, P.; Schuurman, Y. Screening of Bifunctional Water-Gas Shift Catalysts. *Catal. Today* **2008**, *137*, 29–35.

(66) Azzam, K.; Babich, I.; Seshan, K.; Lefferts, L. Bifunctional Catalysts for Single-Stage Water–Gas Shift Reaction in Fuel Cell Applications.: Part 1. Effect of the Support on the Reaction Sequence. *J. Catal.* **2007**, *251*, 153–162.

(67) Kolsbjerg, E. L.; Peterson, A. A.; Hammer, B. Neural-Network-Enhanced Evolutionary Algorithm Applied to Supported Metal Nanoparticles. *Phys. Rev. B* **2018**, *97*, 195424.

(68) Laletina, S. S.; Mamatkulov, M.; Shor, E. A.; Kaichev, V. V.; Genest, A.; Yudanov, I. V.; Rösch, N. Size-Dependence of the Adsorption Energy of CO on Pt Nanoparticles: Tracing Two Intersecting Trends by DFT Calculations. *J. Phys. Chem. C* **2017**, *121*, 17371–17377.